vary dramatically from year to year. Preconditioning of the surface that cold air masses pass over can also influence air-mass evolution, as a recent history of cold conditions or snow cover can enhance the ability of the land surface to act as a heat sink in the development of the coldest air masses (Ellis and Leathers 1998; Gao et al. 2015; Hartig et al. 2023). Intermodel and spatial variability could also result from competing factors, such as the cooling from longwave radiation balanced by warming from turbulent convection identified in Hartig et al. (2023), in a competition that has not fully tipped to either side at the observed level of warming.

The question of cold air outbreaks in a warmer climate is also motivated by the Eocene, a warm climate period that persisted from 56 to 34 million years ago. The Eocene presents a challenge to our understanding of cold air outbreaks in a warmer climate due to strong evidence for the complete suppression of below-freezing temperatures over North America. Estimated $CO_2$ levels during the Eocene range from 600 to over 1500 ppm, depending on the time period and the proxy used (Beerling and Royer 2011; Anagnostou et al. 2020; Rae et al. 2021), and the global mean surface temperature was 10–16 K higher than in the preindustrial climate (Inglis et al. 2020). But wintertime continental interiors were much warmer than they are today. Fossils of frost-intolerant species from the Eocene, including palms, turtles, and crocodiles, have been found in the central Great Plains and Rocky Mountains of North America (Hutchison 1982; Wing and Greenwood 1993; Markwick 1994; Greenwood and Wing 1995). The presence of these species implies no more than a day at a time below freezing and an absolute minimum temperature above −10°C (Wing and Greenwood 1993; Greenwood and Wing 1995; Hyland et al. 2018) with a cold month mean temperature of at least 4°C (Markwick 1994, 1998) and as high as 13°C (Hutchison 1982). Today, those regions have a cold month mean of −4°C and experience over 100 days per year below freezing with typical wintertime minima of −30° to −40°C (NWS 2023), indicating that cold extremes in the Eocene were suppressed by a factor of 2–3 relative to the warming of the wintertime mean.

While multiple lines of fossil evidence point to above-freezing temperatures over Eocene continental interiors, climate models have consistently struggled to simulate conditions that match the proxies. A recent Eocene Model Intercomparison Project noted improvements matching the global mean surface temperature over many models in the project but ongoing issues when comparing to regional climate proxies and did not consider temperature extremes (Lunt et al. 2021). Models that can match high- and midlatitude temperatures produce tropics that are too warm (Shellito et al. 2003) or conversely match the tropics but not higher latitudes (Heinemann et al. 2009). An older CCSM3 model produced reasonable global temperatures but required 4560 ppm $CO_2$ to do so, which the authors interpret as unrealistically low climate sensitivity rather than a challenge to $CO_2$ proxies (Huber and Caballero 2011; Caballero and Huber 2013). The previous generation of Community Earth System Model (CESM) produced a good match for mean annual temperatures across latitudes in the Eocene (Zhu et al. 2019) but did not look at seasonal means or minima. The struggle across many models to simulate a feasible Eocene climate suggests that a deeper understanding of the physical processes that enhance or suppress cold extremes will help identify what is going wrong when models attempt to produce above-freezing continental temperatures in an Eocene-like climate.

In this study, we compare a preindustrial climate scenario to a much warmer climate to understand the physical processes that influence the coldest wintertime temperatures. The warmer climate corresponds to an extension of a high-emissions scenario out to the year 2300 and features a global mean surface temperature of 28.9°C, which is roughly 8 times the preindustrial $CO_2$ level and falls within the range that produced a good match to an Eocene-era climate in CESM1 (Zhu et al. 2019). Our approach combines a calculation of the high-latitude temperature distribution with a temperature budget along air parcel trajectories to analyze the influence of both initial conditions and diabatic evolution on cold air masses across the two scenarios. We observe a sharp drop-off in the wintertime temperature distribution at the freezing temperature, suppressing below-freezing conditions in the warmer climate and above-freezing conditions in the preindustrial case. Using air parcel trajectories, we demonstrate a remarkable similarity in both the dynamics and diabatic effects acting on cold air masses across the two climate scenarios. Cooling from longwave radiation and warming from boundary layer mixing dominate diabatic temperature evolution along cold air outbreak trajectories. Surprisingly, while both diabatic effects strengthen in the warmer climate, the net effect remains the same, around −6 K. By identifying the key physical processes influencing cold air outbreaks and how and why they will change in a warming climate, we hope to improve predictions of when and why North American cold air outbreaks can be expected to decline under anthropogenic climate change and demonstrate how Eocene-like climates could have maintained very warm continental interiors.

## 2. Methods

We approach the evolution of continental cold air outbreaks in a warming climate by comparing a preindustrial to a warmer climate scenario using the CESM2. CESM2 is run at a 0.9° × 1.25° spatial resolution with 32 vertical levels with the Community Atmosphere Model, version 6 (CAM6), and the Community Land Model, version 5 (CLM5). Sea surface temperatures and sea ice coverage are prescribed (described below and shown in Fig. S1 in the online supplemental material). Both scenarios begin with a 2000-era climate (specifically, the F2000climo component set) and then are modified as follows. For the preindustrial scenario, we replace the prescribed year 2000 sea surface temperature and sea ice distributions with those of a preindustrial case, circa 1850, and the atmospheric greenhouse gases (GHGs) with fixed 1850 concentrations. For the year 2300 warmer climate scenario, we prescribe the fixed greenhouse gas concentrations and the sea surface temperature and sea ice distributions using the average over the final decade from the fully coupled run of CESM2 under the shared socioeconomic pathway (SSP) 5-8.5 high-emissions scenario for CMIP6 extended out to the year 2300 (see Figs. S2 and S3

Of particular interest in this study are the factors influencing temperature change within the model. The model temperature tendency at each gridpoint $\dot{T}$ can be decomposed as

$$\dot{T} = \dot{T}_{\text{physics}} + \dot{T}_{\text{dynamics}} + \dot{T}_{\text{fix}}, \tag{1}$$

where $\dot{T}_{\text{physics}}$ is the diabatic tendency from the model physics; $\dot{T}_{\text{dynamics}}$ is calculated by the model's dynamical core and accounts for advection, adiabatic compression and expansion, and the divergence damping (which is expected to be small); and $\dot{T}_{\text{fix}}$ is a very small energy correction, typically $<10^{-4}$ K h$^{-1}$, that ensures the conservation of global energy.

Ultimately, we want to separate the diabatic temperature tendencies $\dot{T}_{\text{physics}}$ from the advective and adiabatic term $\dot{T}_{\text{dynamics}}$. To remove the advective component of the model dynamics term, we use a Lagrangian reference frame by considering temperature tendencies along an air parcel trajectory instead of at a fixed point. To remove the adiabatic component, we transform from temperature to dry static energy, which is conserved under adiabatic motion, as follows:

$$\text{DSE} = c_p T + gz, \tag{2}$$

where $T$ is the temperature, $g$ is the gravitational acceleration, $c_p$ is the specific heat of air, and $z$ is the geopotential height ($z = 0$ at sea level). Whenever we refer to dry static energy throughout the rest of this paper, it is divided by the specific heat of air $c_p$ to give units of temperature. We use dry static energy instead of the more familiar potential temperature because it is the state variable used within CAM6, so many of the temperature tendencies output by the model are in fact internally calculated as dry static energy tendencies and only later converted to temperature space.

These transformations leave us with a dry static energy budget along air parcel trajectories consisting of temperature tendencies from distinct physics processes:

$$\begin{aligned} \dot{\text{DSE}} &= \dot{T}_{\text{physics}} \\ &= \text{BL} + \text{DP} + \text{LW} + \text{SW} + \text{VD} + \text{GW} + \dot{T}_{\text{fix}} \\ &\approx \text{BL} + \text{DP} + \text{LW}, \end{aligned} \tag{3}$$

where BL is boundary layer mixing, DP is deep convection, LW is longwave radiation, SW is shortwave radiation, VD is vertical diffusion, and GW is gravity wave drag. In the final line, we drop the last four terms, which are consistently over an order of magnitude smaller than the leading three terms in the troposphere over North America during winter. We also note that the tendencies due to boundary layer mixing BL and deep convection DP are shorthand for a partitioning of the moist processes temperature tendency within the atmosphere model, $\dot{T}_{\text{moist processes}} = \text{BL} + \text{DP}$, and are used as umbrella terms for a collection of processes. BL refers to the temperature tendency from the Cloud Layers Unified by Binormals (CLUBB) parameterization (Golaz et al. 2002; Bogenschutz et al. 2013) and includes boundary layer turbulence, shallow convection, and latent heat from liquid cloud formation and evaporation, while DP is the remainder of moist processes and includes deep convection, cloud microphysics, and reevaporation of rain and snow.

By integrating over time along a trajectory, we formulate a Lagrangian dry static energy budget that decomposes the total change in dry static energy of the air parcel into the diabatic contributions from distinct model physics processes:

$$\begin{aligned} \Delta\text{DSE} &\approx \int (\text{BL} + \text{DP} + \text{LW})\,dt \\ &= \int \dot{T}_{\text{physics}}\,dt. \end{aligned} \tag{4}$$

## 3. Results

We begin with overall changes to the wintertime temperature distribution over the interior of North America between a preindustrial and a much warmer climate in section 3a. The effect of changes to the climatology and geographical distribution of source regions for cold air masses is considered in section 3b, while the role of diabatic processes acting on those air masses as they are swept over the interior of North America is covered in section 3c.

### a. *Narrowing of the wintertime temperature distribution*

We begin with a consideration of the changes to the wintertime temperature distribution itself when moving from a preindustrial climate to a much warmer climate. Figure 1 shows the December–February distributions of hourly 2-m air temperature over the sampling region in the interior of North America in the preindustrial (blue) and year 2300 (green) modeled climate scenarios. In a warmer climate, the wintertime temperature distribution not only warms but also becomes narrower, with a cold tail that barely drops below freezing. The freezing temperature itself (vertical black line in the figure) helps illustrate the dramatic change between the two scenarios: the wintertime temperature in this region almost never rises above freezing in the preindustrial scenario and almost never drops below freezing in the warmer climate. There is, in fact, a particularly abrupt drop in both scenarios right around freezing. We suggest that this suppression of temperature extremes around the freezing temperature may be a result of the energy consumed by the latent heat of freezing in soil water. Using a range of volumetric heat capacities from $1.5 \times 10^6$ to $3 \times 10^6$ J m$^{-3}$ K to account for variations in soil type and moisture content (Abu-Hamdeh 2003), we find with a back-of-the-envelope calculation (detailed in the supplemental material and Fig. S4) that the top 10 cm of soil contains more than enough water for the latent heat of freezing to entirely offset the surface energy imbalance that accumulates over the 2 days leading up to a typical cold air outbreak. Near-surface air temperatures would thus stall out at the freezing temperature as energy is diverted to melt or freeze water in the soil, reducing the prevalence of above-freezing temperatures in the preindustrial climate and of below-freezing temperatures in the warmer climate. We note that this mechanism assumes efficient energy exchange between the soil surface and the lowest layers of air as well as within the soil to transmit the latent heat of freezing up into contact with overlying air, either of which might be exaggerated in the model to compensate for vertical discretization. One might be able to test this suggested role of latent heat fluxes in shaping the PDF of temperature extremes by examining extreme heat events in present-day regions with a frozen surface and extreme cold in regions with an unfrozen surface, which is beyond the scope of this paper. Further work is required to confirm that the control that the phase change of soil water appears to have on near-surface air temperatures in CESM also operates in the real climate.

The increase in average wintertime temperature between the preindustrial period and our year 2300 scenario, as demonstrated by Fig. 1, is unsurprising. Between a $CO_2$ concentration almost 8 times that of the preindustrial case and a total loss of Arctic sea ice, a wintertime mean temperature of 282 K (9°C, an increase of 21 K relative to preindustrial) for the warmer climate is in line with paleoclimate proxies for the Eocene warm climate period (56–34 Myr) when frost-intolerant species such as crocodiles and palm fronds populated the interior of North America (Hutchison 1982; Wing and Greenwood 1993; Markwick 1994; Greenwood and Wing 1995; Hyland et al. 2018). What is more interesting, at least from a dynamical perspective, is the change in temperature extremes. The fifth percentile of hourly temperature has increased by 27 K between the two scenarios, or 1.3 times the increase in the wintertime mean, while the 95th percentile has increased by only 0.8 times the mean. The amplified warming of cold extremes is consistent with Cronin and Tziperman (2015) who present a low cloud mechanism for suppressing cold air formation in a warmer climate. In our modeled scenarios, cold air outbreaks have indeed warmed by more than both the mean and hot extremes; understanding why this happens is a central goal of this paper.

To understand why wintertime temperature extremes are suppressed in a warmer climate, we consider changes in temperature in terms of two interrelated factors: 1) the location and temperature of source regions for cold air masses and 2) diabatic forcings acting on those air masses as they travel. The diabatic forcings include solar and infrared radiation, latent heating from the condensation or evaporation of water, and boundary fluxes like the surface sensible heat flux. In the shift to a warmer climate, changes to $CO_2$ concentration, atmospheric moisture, clouds, land cover, and precipitation can alter the diabatic forcings acting on an air mass as it travels. Source regions, on the other hand, can be thought of as setting an initial state of temperature and moisture that both are acted upon by and influence diabatic forcings. To a certain extent, one might expect the reduced equator-to-pole temperature gradient during the Eocene, around 15 K versus today's value of 40 K (Zhang et al. 2019), to naturally result in a narrower temperature distribution. If we assume that temperature in one location is primarily constructed from wind-blown temperatures from surrounding locations, then a narrower distribution of temperatures over the globe as a whole would translate naturally to a narrower distribution at some fixed location. However, if diabatic heating and cooling are significant, as has been demonstrated in the case of cold air outbreaks (Hartig et al. 2023), then the temperature of an air mass is modified rather than merely conserved as it is swept about. In our study of cold extremes over the interior of North America, we will therefore consider both changes to the climatology of source regions and changes to diabatic temperature tendencies along airmass trajectories in our attempt to tease out the causes of cold air suppression in a warmer climate.

### b. *A warmer and less stable source region*

Beginning with temperature changes in source regions, we note the dramatic reduction in the frequency of below-freezing days in Arctic source regions between the preindustrial and the year 2300 scenarios illustrated in Fig. 2. The coldest temperatures over the interior of North America in the modern climate usually result from anomalous advection of air masses out of Arctic regions, where dryness and low temperatures set a cold initial state that is enhanced or maintained as these air masses cross the continent (Walsh et al. 2001; Cellitti et al. 2006; Portis et al. 2006; Vavrus et al. 2006; Kolstad et al. 2010; Hankes and Walsh 2011; Smith and Sheridan 2018; Hartig et al. 2023). By using surface dry static energy relative to a reference height of 510 m instead of temperature, we are actually looking at the temperature these air masses would have after the adiabatic compression or expansion due to vertical motions that would accompany advection into the interior of North America (specifically, the gray dashed box in the figure, which has an average surface elevation of 510 m; for the same figure using surface air temperature, see Fig. S5). We leave the consideration of diabatic processes for the second half of this paper. Figure 2 shows a nearly order-of-magnitude reduction in the frequency of below-freezing days over the northernmost parts of North America and a total loss of such conditions over the newly exposed Arctic Ocean in the year 2300 scenario. We also note that Fig. 2 is, if anything, a conservative estimate of the availability of below-freezing air masses for North America. Adiabatic compression will heat any air mass brought to the surface from aloft, so if air masses destined for North America are sourced even a few hundred meters above the surface, then the heating from subsidence can partly or fully counteract the below-freezing initial temperature.

The biggest change in the year 2300 climate scenario other than the increase in $CO_2$ is the complete loss of Arctic sea ice and subsequent dramatic changes in heat and moisture fluxes in the Arctic. With the ocean surface fully exposed, surface sensible heat fluxes into the atmosphere increase by tens of watts per square meter relative to the preindustrial climate, as shown in Fig. 3. The loss of insulating sea ice makes near-surface air over the Arctic Ocean warmer rather than colder than the air bordering continental air and provides a heat source to any air masses passing over it. For instance, while a large number of below-freezing days persist over Siberia in the warmer climate (Fig. 2), any cold air masses originating there would need to pass over open ocean to reach North America, where they would be subject to significant positive surface heat fluxes (Fig. 3).

Given the dramatic changes in the distribution of cold air in the northern high latitudes discussed above, we begin our air parcel trajectory analysis with an investigation into the extent to which the geographical distribution of source regions may

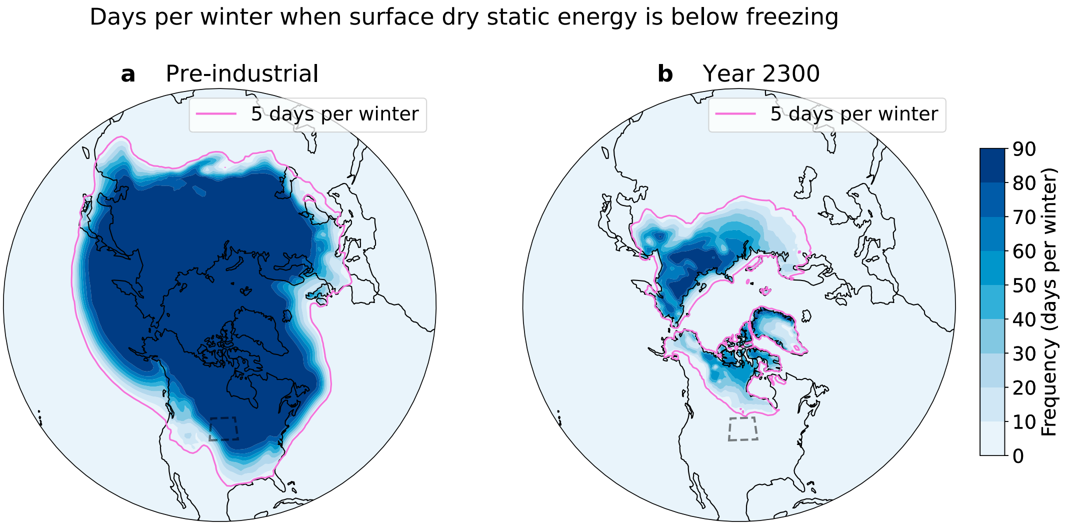

FIG. 2. Reduction in the area below freezing over continental cold air source regions in a warmer climate. Number of days per winter (DJF, averaged over 50 simulated winters) when the average daily surface dry static energy is above freezing. A solid contour has been included in fuchsia marking 5 days per winter to better demarcate the low-frequency regions. Note that, for this figure, dry static energy has been adjusted to a reference height of 510 m instead of sea level such that it reflects the temperature the air parcel would be if raised or lowered adiabatically to the average surface height over interior North America (gray dashed box).

have shifted in the warmer climate. After identifying cold air outbreaks over the interior of North America (gray dashed box), we calculate a 10-day back trajectory for each event (see section 2 for details). The resulting trajectory paths are shown in Fig. 4 for both the preindustrial and year 2300 model scenarios. While a larger fraction of cold air outbreaks pass over the Pacific Ocean in the year 2300 case, it is remarkable how little the source region and airmass trajectories have changed overall. Over half of all trajectories still pass over the Arctic Ocean in the warmer climate scenario, even in spite of the positive heat fluxes (Fig. 3) and dramatically reduced availability of below-freezing days there (Fig. 2). By defining a source region for each climate scenario that contains 90% of all trajectory origin points, we find that the two regions almost fully overlap, with some additional spread of the warmer climate scenario into the Pacific and Russian sectors (see Fig. S6).

At 10 days, back trajectories of midlatitude cold air outbreaks are long enough to sample the source region climatology and strongly reflect changes in source region temperature, as shown in Fig. 5. We find that the 2-m air temperature underlying all trajectory origin points (solid color in Fig. 5) is an excellent match to the climatology of the daily average 2-m air temperature within the source regions defined above (black outline). The peak at 280–284 K in the year 2300 source region climatology which is undersampled by cold air outbreak trajectories corresponds to the Arctic Ocean, where high surface

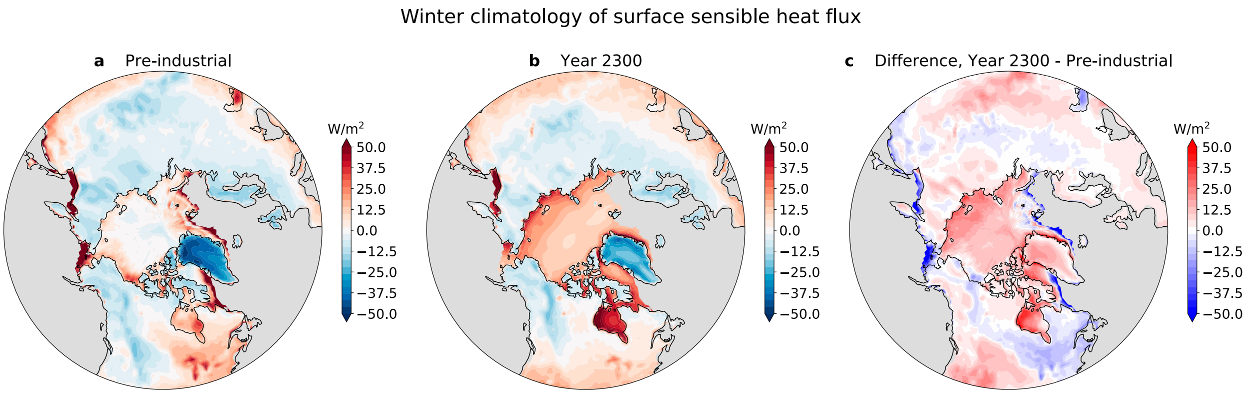

FIG. 3. Changes in surface sensible heat flux with the disappearance of Arctic sea ice. Wintertime climatology over 50 simulated winters of surface sensible heat flux, masked in gray to exclude regions with open ocean in the preindustrial period (both sea ice and land fraction less than 50%). It includes (left) preindustrial model climatology, (center) year 2300, and (right) the difference between the two scenarios. Positive values indicate heat flux from the surface into the atmosphere.

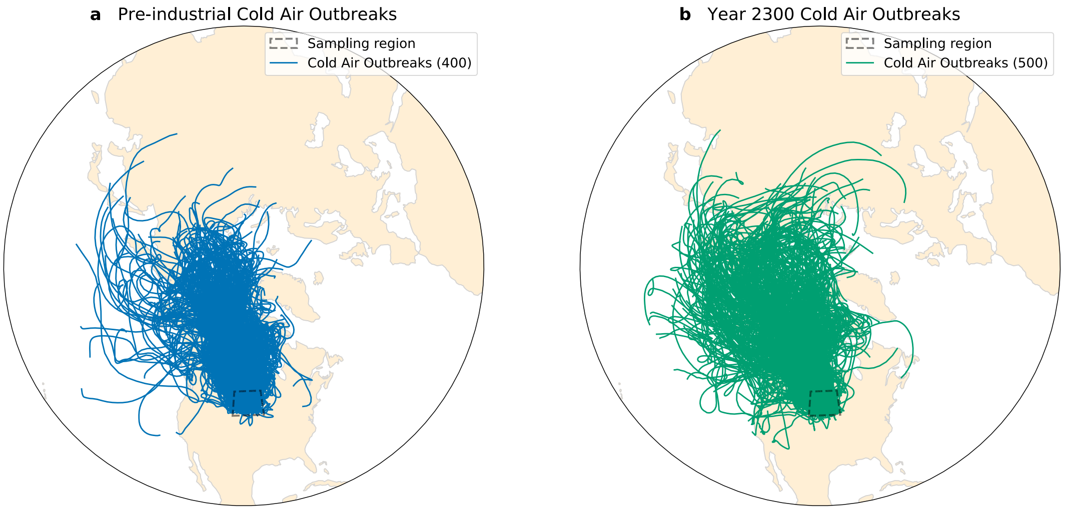

FIG. 4. Back trajectories of cold air outbreaks. Each line represents a 10-day back trajectory initialized from a cold air outbreak identified in the (left) preindustrial (blue) or (right) year 2300 (green) model scenario. The cold air outbreaks used to initialize each trajectory were identified by randomly sampling 400 times (for the preindustrial scenario) or 500 times (for the year 2300 scenario) from the coldest 5% of hourly 2-m air temperatures over 50 simulated winters within the sampling region (black dashed box); see section 2 for more details on the sampling method.

heat fluxes penalize the formation and maintenance of cold air as discussed previously. The change in initial trajectory temperature from the preindustrial to the year 2300 scenario is a direct result of changes to the climatology rather than the location of the source region; the change in the shape of the source region (Fig. S6c) is small enough that we found no significant difference when using the preindustrial versus year 2300 source region to generate the year 2300 climatology.

Another climatological change in the northern high latitudes between the two climate scenarios becomes obvious in the vertical temperature distribution, shown in Fig. 6 as a composite of air columns averaged over all cold air outbreak trajectories. In the preindustrial climate, there is a persistent near-surface temperature inversion in the high latitudes during winter. The presence of the inversion allows cold air outbreak trajectories to stay close to the ground; these near-surface air masses are actually colder than the air aloft, and low sensible heat fluxes along the trajectory paths (Fig. 3a) fail to significantly warm these air masses as they travel out of the Arctic. In the warmer climate, the temperature inversion has disappeared in favor of a steady decline in temperature with height. Positive surface sensible heat fluxes over the Arctic (Fig. 3b) in the first half of the trajectories and cooler temperatures aloft than at the surface mean that cold air outbreak air masses

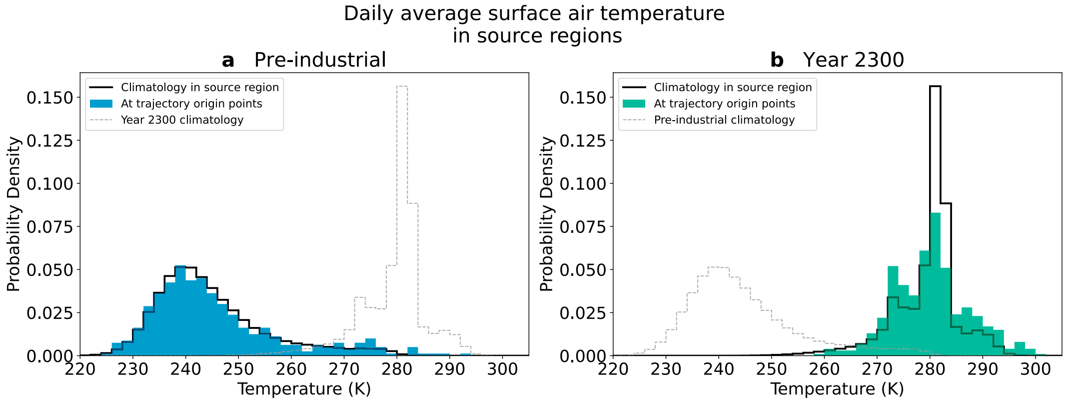

FIG. 5. Trajectories going back 10 days before a midlatitude cold air outbreak sample the wintertime climatology of the source region. Solid colors indicate the distribution of 2-m air temperature underlying all trajectories 10 days before arrival in the midlatitude sampling region for the (a) preindustrial and (b) year 2300 cases. Black contours show the climatology of daily average 2-m air temperature during DJF within the corresponding source region, a polygon that contains 90% of all trajectory origin points (i.e., 10 days before arrival; see supplementary materials for details of source region determination). Dashed contours reproduce the source region climatology of the opposing panel for comparison.

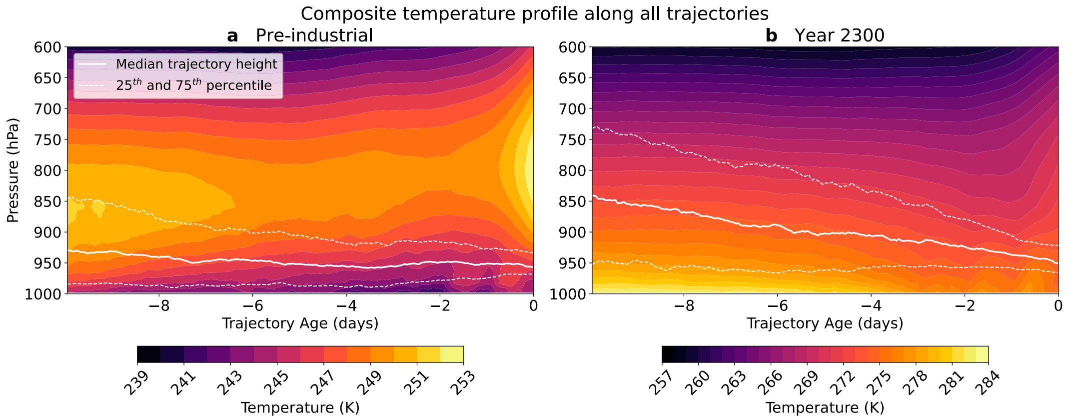

FIG. 6. Loss of the surface temperature inversion along cold air outbreak trajectories. Composites of the vertical temperature profile over all cold air outbreak trajectories (colored lines in Fig. 4) in the (left) preindustrial and (right) year 2300 model scenarios. The $x$ axis is the time along the trajectories in days, where day 0 represents the occurrence of the cold air outbreak in the sampling region. The spread of air parcel trajectory heights within these composite profiles is indicated by a solid white line for the median height and dashed white lines for the 25th–75th percentile range across all trajectories. Note that the contour range is different between the two figures, but the contour spacing is the same (1 K).

originate higher up in the atmosphere in the warmer climate than they do in the preindustrial case. Differences in initial height result in more adiabatic warming for cold air outbreak trajectories in the warmer climate, 9.4 K over 10 days on average, compared to 2.9 K for preindustrial trajectories.

### c. *Enhanced diabatic heating and cooling*

With the initial temperature determined by the climatology in source regions, diabatic heating and cooling provide the final piece to determine temperature evolution as those air masses travel into the midlatitudes. If there is net diabatic heating along a trajectory, it can offset the initially low temperatures of the Arctic air parcel and suppress cold air formation. Conversely, if there is net diabatic cooling, the air mass can become even colder as it travels into the midlatitudes, so diabatic sources are critically important in determining the development of cold air outbreaks.

Using the physics temperature tendencies provided by the atmosphere model, we decompose diabatic temperature evolution along cold air outbreak trajectories into five terms: boundary layer mixing, deep convection, longwave radiation, shortwave radiation, and gravity wave drag. The last two terms, shortwave radiation and gravity wave drag, are more than an order of magnitude smaller than the other components, so we leave them out of the analysis that follows (see Fig. S7 for all components). Additionally, the tendencies due to boundary layer mixing and deep convection are each shorthand for a collection of processes within the atmosphere model that are explained in more detail in section 2. We interpolate each temperature tendency onto the air parcel trajectories and then integrate along each trajectory to get a distribution over all trajectories of the 10-day diabatic temperature tendency attributable to each physical process, shown in Fig. 7.

We note a crucial balance in the diabatic temperature evolution of cold air masses in both the preindustrial and year 2300 climate scenarios. In both scenarios, diabatic temperature evolution is almost entirely dominated by a competition between cooling from longwave radiation (Fig. 7a) and warming from boundary layer mixing (Fig. 7b). The key difference between the two scenarios is that both processes become more intense in the warmer climate; longwave cooling of the air mass is actually stronger in the warmer climate, while boundary layer mixing provides more heating at the parcel level. The two processes nearly cancel out when averaged over all trajectories, but the spread across trajectories is large (see Fig. 7d), indicating that individual trajectories may experience large diabatic temperature changes in either the positive or negative direction. For reference, we note that the fifth percentile of surface temperature is only 7.3 K below the winter average temperature of 282 K over the interior of North America in the year 2300 scenario (Fig. 1), and the surface temperature in source regions is only below freezing a few days every year (Fig. 2). And, while the average diabatic temperature change is just a few degrees, the large spread in Fig. 7 means that most trajectories, in fact, have a nonzero diabatic temperature change (for the full evolution of dry static energy along trajectories, see Fig. S8). While the difference in the temperature of cold air outbreaks between the two climate scenarios is primarily due to changes in the source region temperature, whether a cold air outbreak is produced from an Arctic air mass in a given scenario often comes down to the diabatic temperature change, particularly in the warmer climate (Figs. S8a,b).

The budget residual in Fig. 7e is small for most trajectories. However, there are a handful of trajectories for which it is on par with the total physics temperature tendency Fig. 7d. The trajectories with the largest budget residual have a similar longwave temperature tendency distribution but a larger spread in

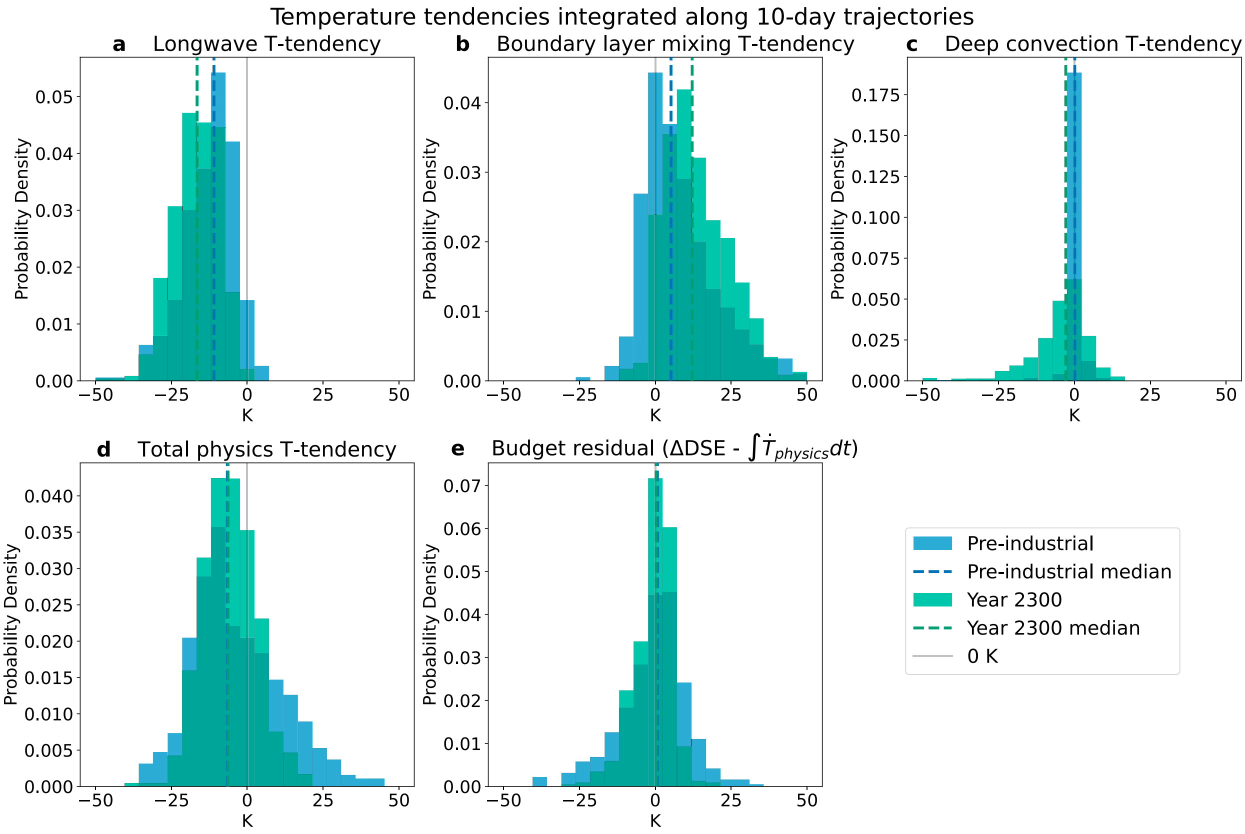

FIG. 7. Contributions to diabatic temperature evolution along cold air outbreak trajectories. Each histogram shows the distribution across all trajectories of the cumulative temperature contribution of a specific model physics process, found by integrating the hourly temperature tendency along each 10-day trajectory. The three largest contributions to the total diabatic temperature evolution are shown along the top row: (a) longwave radiation, (b) boundary layer mixing and latent heat of condensation/evaporation, and (c) deep convection and cloud microphysics. The bottom row shows (d) the total diabatic temperature tendency and (e) the total budget closure residual ($\Delta\mathrm{DSE} - \int \dot{T}_{\mathrm{physics}} dt$), which measures how well changes in dry static energy match up with the diabatic temperature tendencies given by the model.

boundary layer mixing and, therefore, in total physics temperature tendency than those with a small budget residual (not shown). This is consistent with the findings of Hartig et al. (2023), which posited that the budget residual is partly a result of errors introduced in the trajectory calculation in regions with strong vertical temperature or wind gradients.

Two questions naturally arise from the changes in diabatic temperature contributions between the preindustrial and year 2300 scenarios in Figs. 7a and 7b: why does boundary layer mixing lead to more heating in the warmer climate? And why is longwave cooling more intense?

There are two key changes in the warmer climate that can facilitate both heating from boundary layer mixing and cooling from deep convection. The loss of the surface temperature inversion (Fig. 6) removes a major barrier to convection, allowing both shallow and deep convection to proceed more readily. The increase in surface fluxes of heat (Fig. 3) and moisture into the atmosphere inject more heat into the boundary layer and can help fuel convection. Mixing in the boundary layer redistributes those surface fluxes throughout the boundary layer, leading to heating as shown in Figs. 8a and 8b, while deep convection transports surface heat upward into the midtroposphere, leading to cooling in the boundary layer and heating aloft (see Fig. S9 for deep convection profiles). Evidently, more heat is distributed within the boundary layer where most of these trajectories reside than is carried aloft (cooling from deep convection in Fig. 7c for most trajectories is weaker than heating from boundary layer mixing in Fig. 7b), but both processes are enhanced by the loss of the near-surface stable layer and increased surface heat fluxes in the migration from a preindustrial to a warmer climate.

Longwave radiation is the only significant source of diabatic cooling that remains in the warmer climate. Deep convection is just −5 K over 10 days on average in the warmer climate, while boundary layer mixing becomes almost strictly positive. Continental cold air outbreaks, therefore, rely almost entirely on longwave cooling to make or keep Arctic air masses cold into the midlatitudes. The intensification of longwave cooling in the warmer climate is therefore crucial to identifying how cold air outbreaks respond to warming.

We find that the increase in longwave cooling is due primarily to cloud-top radiative cooling between 800 and 900 hPa,

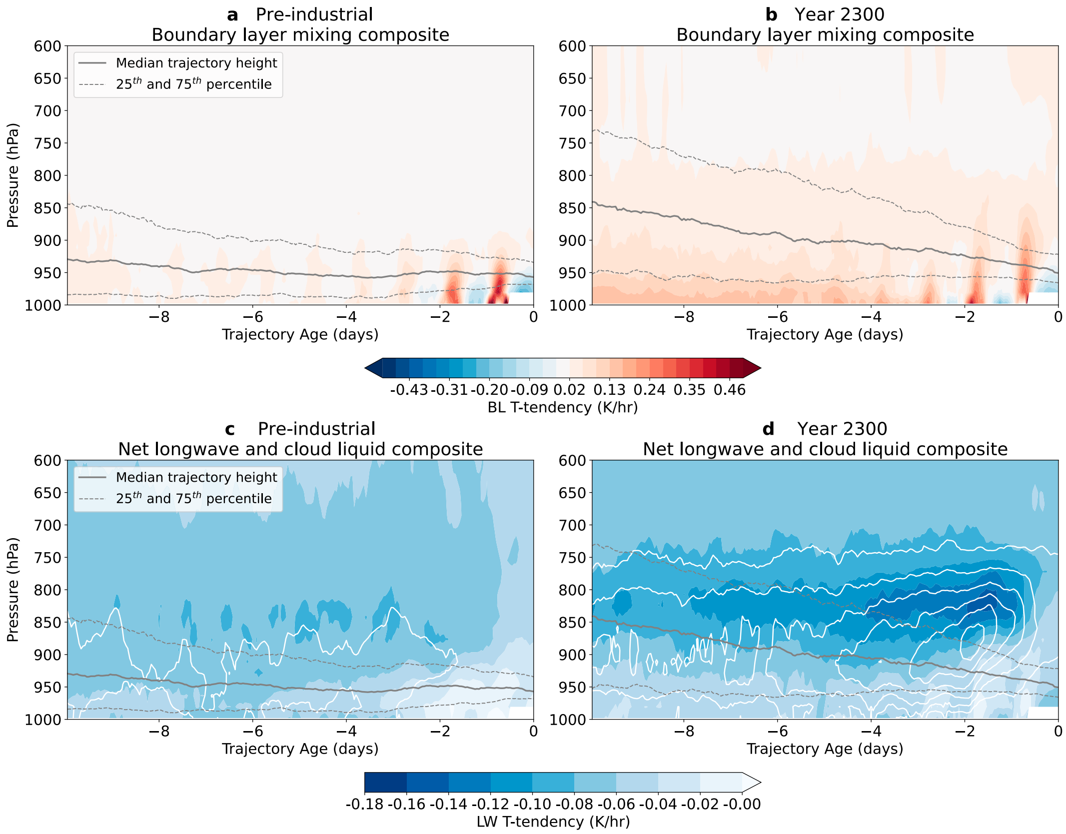

FIG. 8. Boundary layer mixing of greater surface heat flux and cloud-top radiative cooling account for differences in diabatic temperature tendencies. (a),(b) Composites of the boundary layer mixing temperature tendency profiles and (c),(d) longwave temperature tendency (shaded contours) and cloud liquid (solid contours) profiles over all cold air outbreak trajectories (colored paths in Fig. 4) in the (left) preindustrial and (right) year 2300 model scenarios. Gray lines mark the median (solid) and 25th–75th percentile range (dashed) of trajectory heights across all trajectories. Cloud liquid contours start at $1 \times 10^{-5}$ kg kg$^{-1}$ and have a constant spacing of $1 \times 10^{-5}$ kg kg$^{-1}$.

where cold air outbreaks in the warmer climate spend much of their time. Figure 8d demonstrates this effect with composites of cloud liquid and the vertical structure of the longwave temperature tendency along trajectories. In the warmer climate, cloud liquid peaks around 900 hPa and the longwave temperature tendency peaks along the top of the cloud layer between 800 and 850 hPa at values around 0.1 K h$^{-1}$, or upward of 2 K day$^{-1}$. In the preindustrial climate, by contrast (Fig. 8c), cloud liquid is almost an order of magnitude lower and the longwave temperature tendency does not vary much with height. While the magnitude of longwave cooling due to cloud properties depends, in principle, on microphysical cloud processes, Cronin and Tziperman (2015) found a spread of only 5 K across microphysics parameterizations in the 12-day cooling of cold continental air masses with a single-column model, which is considerably less than the spread we observe across our cold air outbreak trajectories (Fig. 7a). The presence of thicker liquid clouds, made possible by higher temperatures and moisture in the warmer climate, increases longwave radiative cooling within the boundary layer and is responsible for more intense longwave radiative cooling along cold air outbreak trajectories.

### d. *Height-dependent pathways to cold air formation*

So far, we have focused primarily on the average behavior of preindustrial versus the year 2300 cold air outbreaks. But there is variation within a single climate scenario as well, as demonstrated by the range of total physics (diabatic) temperature tendencies represented in Fig. 7. The average diabatic temperature change may be −6 K, but some trajectories experience upward of −30 K of cooling, while others have nearly +50 K of warming over the 10 days of travel considered here. To understand what gives rise to this wide range in diabatic temperature change, we subdivide the cold air outbreak trajectories based on their total physics temperature tendencies, constructing two groups representing the extremes of diabatic temperature change to investigate the processes that lead air masses with such different histories to nonetheless result in a midlatitude cold air outbreak.

The comparison of extremes in total diabatic temperature change for the preindustrial climate scenario is displayed in Fig. 9, with trajectories experiencing the most cooling in blue and those experiencing the most warming in red (for similar results from the warmer climate scenario, see Fig. S10). The

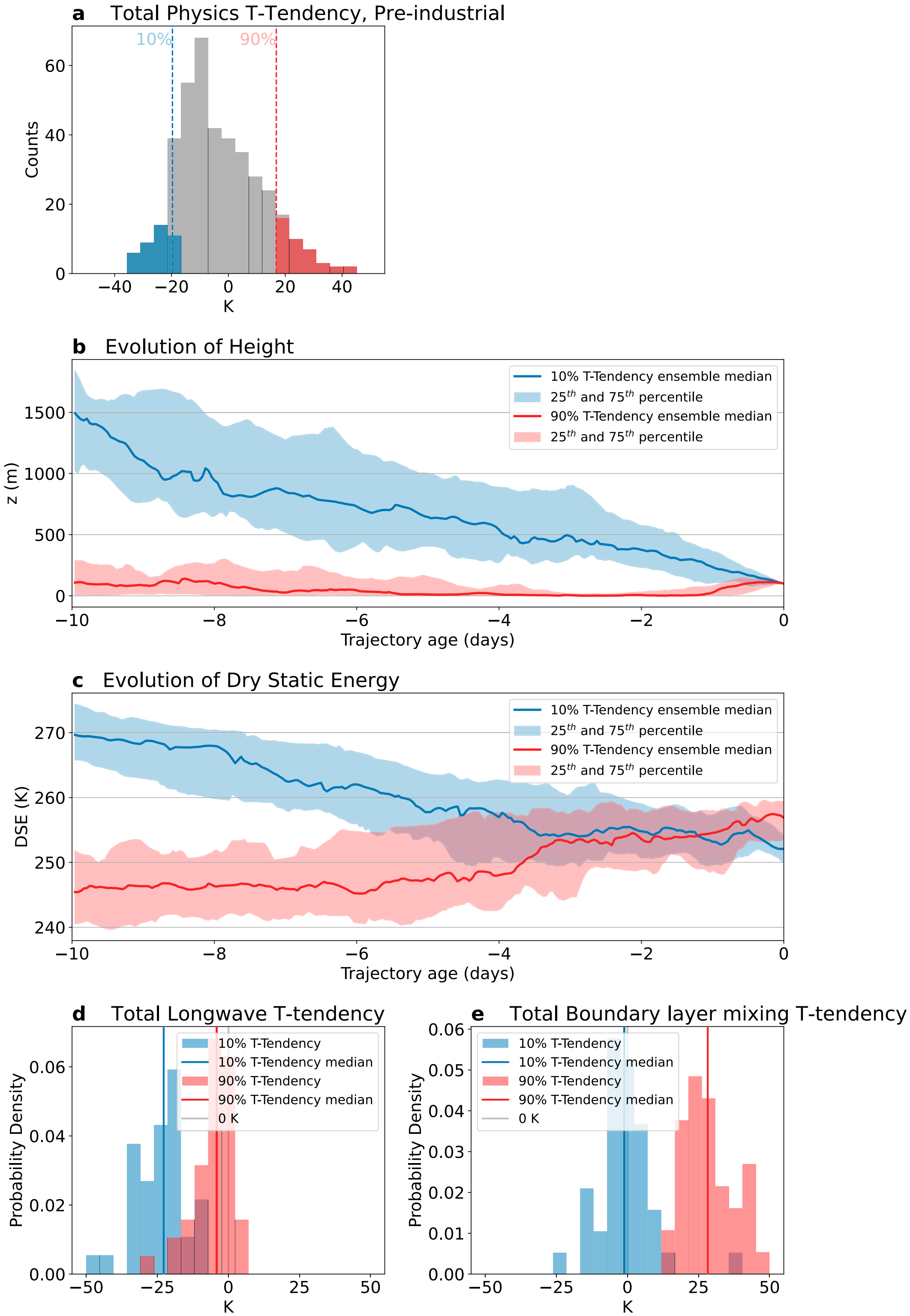

FIG. 9. Trajectories experiencing the most intense diabatic cooling vs heating are primarily differentiated by height. (a) The total physics temperature tendency over all preindustrial cold air outbreak trajectories in gray (same as the blue histogram in Fig. 7d), with trajectories below the 10th percentile marked in blue (10% *T*-Tendency) and those above the 90th percentile in red (90% *T*-Tendency). (b) Evolution of trajectory height along all trajectories in the 10% and 90% *T*-Tendency groups. (c) Evolution of dry static energy along all trajectories in the 10% and 90% *T*-Tendency groups. The total temperature tendency (d) due to longwave radiation and (e) due to boundary layer mixing over all trajectories in the 10% and 90% *T*-Tendency groups.

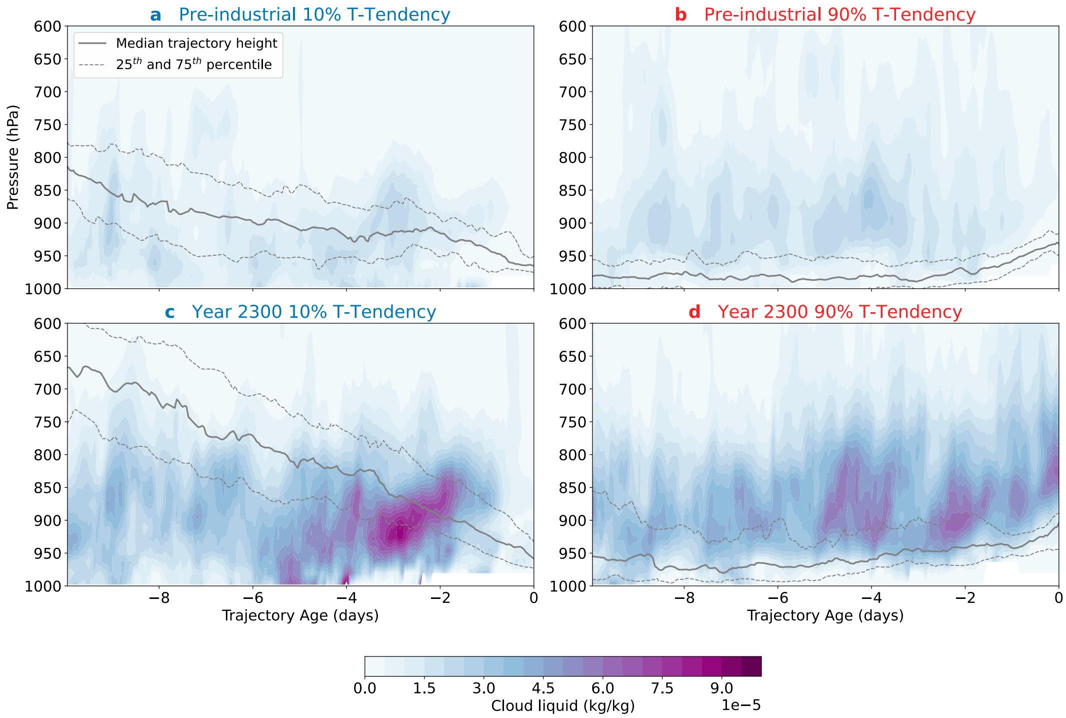

FIG. 10. Cloud conditions are comparable between trajectories that cool intensely and those that warm intensely. Composites of the gridbox cloud liquid over trajectories (a),(c) below the 10th percentile of diabatic temperature tendency and (b),(d) above the 90th percentile. (top) The preindustrial climate scenario and (bottom) the year 2300 scenario.

distinguishing feature is height; comparing Figs. 9b and 9c, we see a compensation whereby trajectories with the most diabatic cooling (blue; decreasing dry static energy) also begin much higher in the atmosphere and therefore adiabatically warm as they descend to the surface. Trajectories with the most warming (red; increasing dry static energy) do the opposite, avoiding adiabatic warming by remaining close to the surface but experiencing diabatic warming as they travel. The two cases meet in the middle in the final few days to produce the same surface temperature distribution. The difference in total diabatic temperature change is reflected in both the longwave cooling and the boundary layer mixing terms, which are more negative for cooling trajectories and more positive for warming trajectories (Figs. 9d,e). But do the differences in diabatic temperature contributions reflect distinct synoptic regimes, or are they merely a consequence of the difference in height?

Figure 10 shows the presence of liquid clouds for the two temperature tendency extremes and both climate scenarios. From an earlier discussion, we know that the longwave radiative effect gets much of its vertical structure from cloud-top radiative cooling (Figs. 8c,d), so here, we use cloud liquid to see if the difference in longwave radiation is a result of distinct cloud regimes for the two cases or merely a consequence of their separation in height. Certainly, the preindustrial climate (top row) has less cloud liquid than the year 2300 climate (bottom row), as discussed in the context of enhanced longwave cooling for Fig. 8. However, within a given climate scenario, we find little difference in the cloud context between the 10% T-Tendency (left column) and the 90% T-Tendency (right column) cases and so conclude that the difference in temperature tendency found in Fig. 9d is because the trajectories with intense cooling travel near the cloud top while those with intense warming travel beneath the cloud layer. The explanation for differences in boundary layer mixing (Fig. 9e) is the same, with trajectories for the two cases merely traveling within different regions of a boundary layer mixing tendency that decreases with height (not shown).

The range of total diabatic temperature change experienced by cold air outbreaks is spanned by differences in trajectory height rather than distinct synoptic conditions. The most intense diabatic cooling tends to occur near the top of the boundary layer, where cloud-top radiative cooling is strong and warming from boundary layer mixing is weak. Air masses that originate higher up in the atmosphere are thus able to cool diabatically by tens of degrees and offset the adiabatic warming that occurs as they descend to the surface. Conversely, air masses that remain close to the ground can afford diabatic warming of tens of degrees and still be very cold by the time they arrive in the continental midlatitudes to produce a cold air outbreak. Even in a much warmer climate, where both longwave cooling and boundary layer mixing produce more intense diabatic temperature change, this range of diabatic pathways for cold air outbreaks is preserved.

## 4. Discussion and conclusions

Wintertime cold air outbreaks affect large swathes of the interior of North America, but their behavior under global warming has proven challenging to predict. In spite of the mean warming trend over the last few decades and its amplification in the Arctic, there is disagreement on whether cold air outbreaks have declined as well. We know that warming wins out eventually because warmer paleoclimate periods like the Eocene (56–34 Mya) present fossil evidence of strong suppression of cold extremes over continental interiors. Therefore, a better understanding of the mechanisms that sustain or suppress cold extremes in a variety of climate states could bolster our knowledge of paleoclimates and improve predictions of temperature extremes under future warming.

In this study, we analyze the development of North American wintertime cold air outbreaks using the CESM2. We compare two climate scenarios with prescribed greenhouse gases, sea surface temperature, and sea ice coverage, corresponding to a preindustrial case and a high-emissions case circa the year 2300, which produces Eocene-like conditions. A midlatitude cold air outbreak may involve some combination of cold initial temperatures in the source region and cooling along the path of travel due to diabatic effects, so we consider both of these factors in our analysis. In the first half of the paper, we analyze climatological differences in cold air outbreak source regions between the preindustrial and the much warmer climate scenarios to quantify the availability of cold air. In the second half, we use a breakdown of the temperature tendencies due to distinct physics processes affecting air parcels as they travel into the midlatitudes to clarify the role of diabatic heating and cooling in turning Arctic air masses into midlatitude cold air outbreaks.

We began this paper by posing two key questions: given the persistence of North American cold air outbreaks observed over the last few decades in spite of an overall warming trend, when and why will they decline as warming continues? And how did much warmer past climates like the Eocene, which may serve as an analog for warmer future climates, so effectively suppress below-freezing temperatures over continental interiors? In the process of addressing these questions below, we highlight our three main results: 1) the latent heat of freezing suppresses warm extremes in a preindustrial climate and cold extremes in a much warmer climate; 2) the transition to a warmer climate, and in particular the loss of Arctic sea ice and the near-surface temperature inversion at high latitudes, dramatically decreases the availability of below-freezing air, suppressing midlatitude cold extremes; and 3) while the net diabatic temperature change along cold air outbreak trajectories is nearly identical between the preindustrial and the much warmer climate, the primary heating and cooling mechanisms both get stronger in the warmer climate.

Based on wintertime temperature distributions over the interior of North America, we determined that the latent heat of freezing serves as a significant barrier to extreme temperatures in both climate scenarios. In a warmer climate, where wintertime surface temperatures are generally above freezing, liquid water in surface soils has the potential to release enough heat through freezing to offset the energy lost to surface sensible heat flux as a cold airmass approaches, preventing surface temperatures from dropping below freezing. The converse occurs in a cold climate, as ice near the surface can absorb excess heat through melting and resist the formation of above-freezing air. Both effects are visible in the sharp drop of the wintertime temperature distribution at freezing (Fig. 1), shortening the warm tail of the preindustrial distribution and suppressing below-freezing temperatures in the warmer climate. The potential role of the latent heat of freezing implies that the availability of surface and soil water can have an important mitigating effect on the development of temperature extremes near the freezing temperature. The mitigating effect of latent heat from soil water also indicates that using a slab surface with static material properties, as done in single-column studies of airmass transformations such as Curry (1983) and Cronin and Tziperman (2015), neglects a potentially important role for evolving surface properties in setting near-surface air temperature.

It is difficult to confirm the role of the latent heat of freezing directly with the trajectory approach we have chosen due to a selection effect. Because this study focuses on air masses that become cold air outbreaks, our study sample would not generally include those air masses that are prevented from becoming cold air outbreaks in the much warmer climate due to exposure to the enhanced surface heat fluxes that could arise from freezing surface water. We do have two results from the warmer climate which are at least consistent with this theory. First, the temperature tendency due to boundary layer mixing is much higher among cold air outbreaks that travel near the surface in the warmer climate, consistent with increased surface sensible heat flux (Fig. S10e). Second, cold air outbreak trajectories originate higher up in the air column (Fig. 6a vs Fig. 6b), likely because they are less exposed to increased surface heat fluxes there. To confirm that the surface heat flux is both anomalous and a result of the latent heat of freezing from surface water, one could look in detail at the behavior of soil moisture in the land model or compare surface heat fluxes along trajectories from the cold tail to the rest of the temperature distribution, but those are beyond the scope of this paper.

The rest of the suppression of extremely cold temperatures, beyond the role we envision for latent heat flux in preconditioning the surface as discussed above, can be attributed to the disproportionate increase in Arctic temperatures that accompanies Arctic amplification and the adiabatic warming that results from changes in vertical temperature distribution. We have determined that the net diabatic cooling is largely unchanged in the transition from a preindustrial to a much warmer climate, and so increases in temperature in the source region and adiabatic warming along the air-mass trajectory are responsible for the narrowing of the wintertime surface temperature distribution demonstrated in Fig. 1, consistent with the Eocene fossil evidence. We note that this conclusion was not inevitable; there was no reason to assume a priori that the diabatic temperature tendency would not change in a radically warmer climate scenario, and in fact, Hartig et al. (2023) demonstrated that the diabatic cooling that occurs in a preindustrial climate is essential to producing midlatitude cold air outbreaks. For precisely this reason, we also emphasize our finding that the suppression of cold air outbreaks arises from a combination of key factors. A considerable number of climate features had to change to produce the adiabatic, diabatic, and source region temperature changes that suppress cold air outbreaks in a warmer climate: loss of the near-surface temperature inversion and static stability, the retreat of Arctic sea ice, and increased low-level liquid clouds. In the near future, or possibly even in present trends, we may observe these changes piecemeal and therefore see either enhancement or suppression of cold air outbreaks in the short term.

The transition to a warmer climate is also accompanied by a marked decrease in the availability of below-freezing air in the Arctic source region, a result of changes to a handful of key climatological features. Increased heat fluxes from the ocean to the atmosphere at high latitudes (Fig. 3), a result of the disappearance of Arctic sea ice in the warmer climate, raise surface temperatures over the Arctic Ocean above freezing, dramatically reducing the availability of below-freezing air near the surface (Fig. 2). The near-surface temperature inversion, present throughout the winter at high latitudes in the preindustrial climate, also disappears in the warmer climate (Fig. 6), a manifestation of Arctic amplification. This removes the layer of stable, cold, dry air near the surface that supplied most of the cold air masses in the preindustrial case. It also presents an avenue to predicting the decline of cold air outbreaks in the near future: Arctic sea ice and the near-surface temperature inversion are crucial to supplying the extremely cold air masses that can turn into midlatitude cold air outbreaks. Disruptions to either of those features are likely to result in a significant shift in the availability of cold air masses.

Given the dramatic changes to temperature and stability in source regions that accompany the transition to a warmer climate, it is remarkable how little the dynamics and net diabatic effects were found to change. Cold air outbreak trajectories are less heavily clustered over the Arctic Ocean in the warmer climate relative to the preindustrial case, but over half still pass over it on their way to the midlatitudes (Fig. 4) and the source region for cold air outbreaks merely expands a bit into the Pacific and toward Russia in the transition to a warmer climate (Fig. S6). The Arctic Ocean and its surrounding environs therefore continue to serve as the primary source region for cold air outbreaks. The net diabatic temperature change along trajectories is also nearly identical, at −6.5 K for the preindustrial and −6.3 K for the warmer climate.

The similarity in net diabatic effect across the two climate scenarios would be surprising in its own right considering all of the changes to atmospheric temperature and moisture that accompany the shift to an Eocene-like climate but is even more remarkable given the changes to two of the largest contributors to diabatic temperature change: longwave radiation and boundary layer mixing (Fig. 7). Longwave cooling is more intense in the warmer climate due to enhanced cloud-top radiative cooling (Figs. 8c,d), while warming from boundary layer mixing is also stronger and reflects more effective redistribution of enhanced surface sensible heat fluxes (Figs. 8a,b). While the net effect is the same for the preindustrial and the warmer climate, the distribution of total physics temperature tendency is narrower (Fig. 7d), which could reflect a greater correlation between the two competing effects via convection. Our results share some similarities with the single-column model study of Cronin and Tziperman (2015), as we see an enhancement of continental low cloud cover as cold air masses move over the continent in the warmer climate. However, the net diabatic cooling along trajectories is only about half of the rate observed by Cronin and Tziperman (2015), possibly because our trajectories descend below the cloud layer and are subject to heating from boundary layer mixing that is reduced in Cronin and Tziperman (2015) by the lack of solar insolation. Our results also have implications for the challenges encountered by climate models attempting to represent cold air suppression in Eocene-like continental interiors. The enhancement of both the longwave and boundary layer mixing temperature tendencies in the warmer climate is primarily a result of cloud and convection processes, which are notoriously tricky to simulate. Models may be missing or misrepresenting key elements of these processes in the extreme conditions of a much warmer climate, where we have few modern analogs with which to develop and test parameterizations.

We note some key differences from the conclusions of Hartig et al. (2023), which used a similar methodology to the one employed here to look at the diabatic processes leading some but not other Arctic air masses to result in midlatitude cold air outbreaks in a preindustrial climate scenario. Hartig et al. (2023) also found the total diabatic temperature change to be a competition primarily between longwave radiation and vertical mixing, but in that study, the contribution of the vertical mixing term is negative on average for cold air outbreak trajectories (while here we find it to be positive on average, see Fig. 7b), producing a net diabatic cooling of −10 K rather than the −6 K reported here. The average temperature tendency due to vertical mixing found for preindustrial cold air outbreaks in Hartig et al. (2023), −3.5 ± 11 K, is about one standard deviation below the value found for boundary layer mixing in this study, 8.3 ± 13 K. This discrepancy is most likely the result of several key changes to CESM that occurred between version 1, used in Hartig et al. (2023), and version 2, used here. The vertical mixing parameterization used in earlier versions of the atmosphere model such as CAM5 was entirely replaced with the CLUBB boundary layer mixing scheme introduced in CAM6 (Golaz et al. 2002; Bogenschutz et al. 2013). Along with adjustments made in the next generation of both the land model and the sea ice model (which is used even in the prescribed sea ice configuration to calculate surface heat fluxes and temperature over sea ice), the surface sensible heat flux underlying cold air outbreak trajectories has increased by about 10 W $m^{-2}$, tipping the average temperature tendency due to boundary layer mixing from slightly negative to slightly positive [cf. Fig. 6a of Hartig et al. (2023) to Fig. S11c]. While Arctic cloud properties and surface air temperature are significantly improved in the newer version of CESM using CLUBB (McIlhattan et al. 2020; Baek et al. 2022), the wintertime surface air temperature bias in the midlatitudes has merely changed sign from negative to positive (Danabasoglu et al. 2020). CLUBB certainly represents a more internally consistent representation of boundary layer mixing, but its effect on temperature tendencies has not been evaluated directly, so it is unclear which version is more realistic for cold air outbreak development.

When considering the scope and implications of this work, it is important to keep in mind several caveats. We note that our warmer climate scenario, intended to emulate the year 2300 of an extended high emissions run of CESM, is not a direct simulation of the Eocene itself but rather evocative of much warmer climates. By using a 2000-era model configuration as a starting point, we incorporate modern vegetation, land ice, and topography while setting greenhouse gases to match projected anthropogenic emissions. We chose these conditions in pursuit of a signal in the occurrence and characteristics of cold events that is strong enough to be differentiated from that of the preindustrial scenario and to allow for attribution to changes in radiative forcing, sea ice, and sea surface temperature rather than variable vegetation and topographic effects, which we feel was largely successful. There are also limitations to the interpretability of our trajectory analysis, which are also discussed in detail in Hartig et al. (2023) but will be restated here. We chose the cold event sampling region from which back trajectories are started based on its continental climate, the existence of extreme cold events at present, and the relevance to Eocene proxy observations. This choice allowed us to isolate the drivers of variability and change in cold air formation for this region, but it also means that our results may not generalize to other environments. One could use a similar methodology in different regions, but it is difficult to speculate how similar the results would be for a region that is closer to the ocean, for example. Additionally, the diabatic temperature budget residual for a Lagrangian trajectory, which should be zero, is near zero for the majority of trajectories but upward of 10 K for a handful in both climate scenarios (Fig. 7e). We attribute these residuals (budget errors) primarily to the effect of vertical positioning errors in HYSPLIT that are further exaggerated by the strong vertical temperature gradients in near-surface wintertime inversions. This is consistent with the reduced error in the warmer climate scenario where vertical temperature gradients are smaller due to the loss of the near-surface temperature inversion. As the median residual for both scenarios is zero, our focus remains on the differences in temperature tendency between the two scenarios and the physical mechanisms we can identify that explain those differences. With our method, we are able to quantify the residual itself rather than attributing it to a collection of physical processes that do not have an explicit temperature tendency as is more commonly done.

Ultimately, we have developed a mechanistic understanding of North American cold air outbreaks and how they might change in a warmer climate. Both the availability of cold air in high-latitude source regions and diabatic effects acting on heat or cool air masses as they travel into the midlatitudes can affect the development of wintertime cold extremes. The median diabatic cooling is −6 K for air parcels traveling toward cold events. But it ranges into tens of degrees for many trajectories, so diabatic effects often play a major role in the evolution of Arctic air masses in both the preindustrial and the much warmer climate scenario. Since the net diabatic effect is the same in the two scenarios, we find that the decreased availability of cold air in the Arctic in a warmer climate is sufficient to suppress below-freezing temperatures over the interior of North America in spite of the persistence of diabatic cooling along air parcel trajectories in the warmer climate scenario. To understand and predict changes to cold air outbreaks in a warming world, we must therefore account for changes to both source regions and diabatic processes, as either can tip the scale in controlling whether an Arctic air mass becomes a cold air outbreak when swept into the midlatitudes.

*Acknowledgments.* This work was funded by NSF Grant 2303486 from the P4CLIMATE program. KH is funded by a National Defense Science and Engineering Graduate (NDSEG) Fellowship. The authors thank Rodrigo Caballero, Peter Hitchcock, and an anonymous reviewer for their comments and suggestions, which improved the paper. ET thanks the Weizmann Institute for its hospitality during parts of this work. Computing and data storage resources, including the Cheyenne supercomputer (https://doi.org/10.5065/D6RX99HX), were provided by the Computational and Information Systems Laboratory (CISL) at NCAR. NCAR is sponsored by the National Science Foundation. Special thanks to Brian Medeiros for help with the CAM6 temperature budget and setting up fixed GHG runs in CESM2 and to Adam Herrington for a breakdown of the processes covered by CLUBB in CAM6.

*Data availability statement.* Simulations were performed using CESM2.1.3 with CAM6, which is freely available at https://www.cesm.ucar.edu/models/cesm2 following registration. The CESM2-WACCM output used to generate prescribed SST and sea ice files for the year 2300 scenario is available at http://doi.org/10.22033/ESGF/CMIP6.10115 under the ssp585 tag. Fixed greenhouse gas concentrations for the year 2300 scenario come from Meinshausen et al. (2020). Back trajectories were calculated using HYSPLIT, version 5.1.0 [with modifications described in Hartig et al. (2023)], which is freely available at https://www.ready.noaa.gov/HYSPLIT.php. The code used to interpolate CAM data onto HYSPLIT trajectories is available on GitHub at https://github.com/kahartig/camtrack.

## REFERENCES

Abu-Hamdeh, N. H., 2003: Thermal properties of soils as affected by density and water content. *Biosyst. Eng.*, **86**, 97–102, https://doi.org/10.1016/S1537-5110(03)00112-0.

Anagnostou, E., and Coauthors, 2020: Proxy evidence for state-dependence of climate sensitivity in the Eocene greenhouse. *Nat. Commun.*, **11**, 4436, https://doi.org/10.1038/s41467-020-17887-x.

Arias, P. A., and Coauthors, 2021: Technical summary. *Climate Change 2021: The Physical Science Basis*, V. Masson-Delmotte et al., Eds., Cambridge University Press, 33–144.

Baek, E.-H., J. Bae, H.-J. Sung, E. Jung, B.-M. Kim, and J.-H. Jeong, 2022: Characteristics of high-latitude climate and cloud simulation in Community Atmospheric Model version 6 (CAM6). *Atmosphere*, **13**, 936, https://doi.org/10.3390/atmos13060936.

Beerling, D. J., and D. L. Royer, 2011: Convergent CENOZOIC $CO_2$ history. *Nat. Geosci.*, **4**, 418–420, https://doi.org/10.1038/ngeo1186.

Bogenschutz, P. A., A. Gettelman, H. Morrison, V. E. Larson, C. Craig, and D. P. Schanen, 2013: Higher-order turbulence closure and its impact on climate simulations in the Community Atmosphere Model. *J. Climate*, **26**, 9655–9676, https://doi.org/10.1175/JCLI-D-13-00075.1.

Caballero, R., and M. Huber, 2013: State-dependent climate sensitivity in past warm climates and its implications for future climate projections. *Proc. Natl. Acad. Sci. USA*, **110**, 14 162–14 167, https://doi.org/10.1073/pnas.1303365110.

Cellitti, M. P., J. E. Walsh, R. M. Rauber, and D. H. Portis, 2006: Extreme cold air outbreaks over the United States, the polar vortex, and the large-scale circulation. *J. Geophys. Res.*, **111**, D02114, https://doi.org/10.1029/2005JD006273.

Cohen, J., and D. Entekhabi, 1999: Eurasian snow cover variability and Northern Hemisphere climate predictability. *Geophys. Res. Lett.*, **26**, 345–348, https://doi.org/10.1029/1998GL900321.

——, and Coauthors, 2014: Recent Arctic amplification and extreme mid-latitude weather. *Nat. Geosci.*, **7**, 627–637, https://doi.org/10.1038/ngeo2234.

Cronin, T. W., and E. Tziperman, 2015: Low clouds suppress Arctic air formation and amplify high-latitude continental winter warming. *Proc. Natl. Acad. Sci. USA*, **112**, 11 490–11 495, https://doi.org/10.1073/pnas.1510937112.

Curry, J., 1983: On the formation of continental polar air. *J. Atmos. Sci.*, **40**, 2278–2292, https://doi.org/10.1175/1520-0469(1983)040<2278:OTFOCP>2.0.CO;2.

Danabasoglu, G., and Coauthors, 2020: The Community Earth System Model version 2 (CESM2). *J. Adv. Model. Earth Syst.*, **12**, e2019MS001916, https://doi.org/10.1029/2019MS001916.

Draxler, R. R., 1999: HYSPLIT 4 user's guide. NOAA Tech. Rep. ERL ARL-230, NOAA/Air Resources Laboratory, 38 pp.

——, and G. D. Hess, 1997: Description of the HYSPLIT_4 modeling system. NOAA Tech. Memo. ERL ARL-224, NOAA Air Resources Laboratory, 31 pp.

——, and ——, 1998: An overview of the HYSPLIT_4 Modelling System for trajectories, dispersion, and deposition. *Aust. Meteor. Mag.*, **47**, 295–308.

Ellis, A. W., and D. J. Leathers, 1998: A quantitative approach to evaluating the effects of snow cover on cold airmass temperatures across the U.S. Great Plains. *Wea. Forecasting*, **13**, 688–701, https://doi.org/10.1175/1520-0434(1998)013<0688:AQATET>2.0.CO;2.

Gao, Y., L. R. Leung, J. Lu, and G. Masato, 2015: Persistent cold air outbreaks over North America in a warming climate. *Environ. Res. Lett.*, **10**, 044001, https://doi.org/10.1088/1748-9326/10/4/044001.

Golaz, J.-C., V. E. Larson, and W. R. Cotton, 2002: A PDF-based model for boundary layer clouds. Part I: Method and model description. *J. Atmos. Sci.*, **59**, 3540–3551, https://doi.org/10.1175/1520-0469(2002)059<3540:APBMFB>2.0.CO;2.

Gong, G., D. Entekhabi, and J. Cohen, 2003: Modeled Northern Hemisphere winter climate response to realistic Siberian snow anomalies. *J. Climate*, **16**, 3917–3931, https://doi.org/10.1175/1520-0442(2003)016<3917:MNHWCR>2.0.CO;2.

Greenwood, D. R., and S. L. Wing, 1995: Eocene continental climates and latitudinal temperature gradients. *Geology*, **23**, 1044–1048, https://doi.org/10.1130/0091-7613(1995)023<1044:ECCALT>2.3.CO;2.

Grotjahn, R., and Coauthors, 2016: North American extreme temperature events and related large scale meteorological patterns: A review of statistical methods, dynamics, modeling, and trends. *Climate Dyn.*, **46**, 1151–1184, https://doi.org/10.1007/s00382-015-2638-6.

Hankes, I. E., and J. E. Walsh, 2011: Characteristics of extreme cold air masses over the North American sub-Arctic. *J. Geophys. Res.*, **116**, D11102, https://doi.org/10.1029/2009JD013582.

Hartig, K., E. Tziperman, and C. P. Loughner, 2023: Processes contributing to North American cold air outbreaks based on air parcel trajectory analysis. *J. Climate*, **36**, 931–943, https://doi.org/10.1175/JCLI-D-22-0204.1.

Heinemann, M., J. H. Jungclaus, and J. Marotzke, 2009: Warm Paleocene/Eocene climate as simulated in ECHAM5/MPI-OM. *Climate Past*, **5**, 785–802, https://doi.org/10.5194/cp-5-785-2009.

Huber, M., and R. Caballero, 2011: The early Eocene equable climate problem revisited. *Climate Past*, **7**, 603–633, https://doi.org/10.5194/cp-7-603-2011.

Hurrell, J. W., J. J. Hack, D. Shea, J. M. Caron, and J. Rosinski, 2008: A new sea surface temperature and sea ice boundary dataset for the Community Atmosphere Model. *J. Climate*, **21**, 5145–5153, https://doi.org/10.1175/2008JCLI2292.1.

Hutchison, J. H., 1982: Turtle, crocodilian, and champsosaur diversity changes in the Cenozoic of the north-central region of western United States. *Palaeogeogr. Palaeoclimatol. Palaeoecol.*, **37**, 149–164, https://doi.org/10.1016/0031-0182(82)90037-2.

Hyland, E. G., K. W. Huntington, N. D. Sheldon, and T. Reichgelt, 2018: Temperature seasonality in the North American continental interior during the Early Eocene Climatic Optimum. *Climate Past*, **14**, 1391–1404, https://doi.org/10.5194/cp-14-1391-2018.

Inglis, G. N., and Coauthors, 2020: Global mean surface temperature and climate sensitivity of the early Eocene Climatic Optimum (EECO), Paleocene–Eocene Thermal Maximum (PETM), and latest Paleocene. *Climate Past*, **16**, 1953–1968, https://doi.org/10.5194/cp-16-1953-2020.

Kolstad, E. W., T. Breiteig, and A. A. Scaife, 2010: The association between stratospheric weak polar vortex events and cold air outbreaks in the Northern Hemisphere. *Quart. J. Roy. Meteor. Soc.*, **136**, 886–893, https://doi.org/10.1002/qj.620.

Liu, J., J. A. Curry, H. Wang, M. Song, and R. M. Horton, 2012: Impact of declining Arctic sea ice on winter snowfall. *Proc. Natl. Acad. Sci. USA*, **109**, 4074–4079, https://doi.org/10.1073/pnas.1114910109.

Lunt, D. J., and Coauthors, 2021: DeepMIP: Model intercomparison of Early Eocene Climatic Optimum (EECO) large-scale climate features and comparison with proxy data. *Climate Past*, **17**, 203–227, https://doi.org/10.5194/cp-17-203-2021.

Markwick, P. J., 1994: "Equability," continentality, and Tertiary "climate": The crocodilian perspective. *Geology*, **22**, 613–616, https://doi.org/10.1130/0091-7613(1994)022<0613:ECATCT>2.3.CO;2.

——, 1998: Fossil crocodilians as indicators of Late Cretaceous and Cenozoic climates: Implications for using palaeontological data in reconstructing palaeoclimate. *Palaeogeogr. Palaeoclimatol. Palaeoecol.*, **137**, 205–271, https://doi.org/10.1016/S0031-0182(97)00108-9.

McIlhattan, E. A., J. E. Kay, and T. S. L'Ecuyer, 2020: Arctic clouds and precipitation in the Community Earth System

Model version 2. *J. Geophys. Res. Atmos.*, **125**, e2020JD032521, https://doi.org/10.1029/2020JD032521.

Meinshausen, M., and Coauthors, 2020: The shared socio-economic pathway (SSP) greenhouse gas concentrations and their extensions to 2500. *Geosci. Model Dev.*, **13**, 3571–3605, https://doi.org/10.5194/gmd-13-3571-2020.

NWS, 2023: Nowdata climate for western and central Wyoming. NOAA/National Weather Service, accessed 10 August 2023, https://www.weather.gov/wrh/Climate?wfo=riw.

Portis, D. H., M. P. Cellitti, W. L. Chapman, and J. E. Walsh, 2006: Low-frequency variability and evolution of North American cold air outbreaks. *Mon. Wea. Rev.*, **134**, 579–597, https://doi.org/10.1175/MWR3083.1.

Rae, J. W., Y. G. Zhang, X. Liu, G. L. Foster, H. M. Stoll, and R. D. M. Whiteford, 2021: Atmospheric $CO_2$ over the past 66 million years from marine archives. *Annu. Rev. Earth Planet. Sci.*, **49**, 609–641, https://doi.org/10.1146/annurev-earth-082420-063026.

Robeson, S. M., C. J. Willmott, and P. D. Jones, 2014: Trends in hemispheric warm and cold anomalies. *Geophys. Res. Lett.*, **41**, 9065–9071, https://doi.org/10.1002/2014GL062323.

Screen, J. A., 2014: Arctic amplification decreases temperature variance in northern mid- to high-latitudes. *Nat. Climate Change*, **4**, 577–582, https://doi.org/10.1038/nclimate2268.

Shellito, C. J., L. C. Sloan, and M. Huber, 2003: Climate model sensitivity to atmospheric $CO_2$ levels in the Early–Middle Paleogene. *Palaeogeogr. Palaeoclimatol. Palaeoecol.*, **193**, 113–123, https://doi.org/10.1016/S0031-0182(02)00718-6.

Smith, E. T., and S. C. Sheridan, 2018: The characteristics of extreme cold events and cold air outbreaks in the eastern United States. *Int. J. Climatol.*, **38**, e807–e820, https://doi.org/10.1002/joc.5408.

——, and ——, 2020: Where do cold air outbreaks occur, and how have they changed over time? *Geophys. Res. Lett.*, **47**, e2020GL086983, https://doi.org/10.1029/2020GL086983.

Stein, A. F., R. R. Draxler, G. D. Rolph, B. J. B. Stunder, M. D. Cohen, and F. Ngan, 2015: NOAA's HYSPLIT atmospheric transport and dispersion modeling system. *Bull. Amer. Meteor. Soc.*, **96**, 2059–2077, https://doi.org/10.1175/BAMS-D-14-00110.1.

van Oldenborgh, G. J., E. Mitchell-Larson, G. A. Vecchi, H. de Vries, R. Vautard, and F. Otto, 2019: Cold waves are getting milder in the northern midlatitudes. *Environ. Res. Lett.*, **14**, 114004, https://doi.org/10.1088/1748-9326/ab4867.

Vavrus, S., 2007: The role of terrestrial snow cover in the climate system. *Climate Dyn.*, **29**, 73–88, https://doi.org/10.1007/s00382-007-0226-0.

——, J. E. Walsh, W. L. Chapman, and D. Portis, 2006: The behavior of extreme cold air outbreaks under greenhouse warming. *Int. J. Climatol.*, **26**, 1133–1147, https://doi.org/10.1002/joc.1301.

Vavrus, S. J., F. Wang, J. E. Martin, J. A. Francis, Y. Peings, and J. Cattiaux, 2017: Changes in North American atmospheric circulation and extreme weather: Influence of Arctic amplification and Northern Hemisphere snow cover. *J. Climate*, **30**, 4317–4333, https://doi.org/10.1175/JCLI-D-16-0762.1.

Walsh, J. E., A. S. Phillips, D. H. Portis, and W. L. Chapman, 2001: Extreme cold outbreaks in the United States and Europe, 1948–99. *J. Climate*, **14**, 2642–2658, https://doi.org/10.1175/1520-0442(2001)014<2642:ECOITU>2.0.CO;2.

Westby, R. M., Y.-Y. Lee, and R. X. Black, 2013: Anomalous temperature regimes during the cool season: Long-term trends, low-frequency mode modulation, and representation in CMIP5 simulations. *J. Climate*, **26**, 9061–9076, https://doi.org/10.1175/JCLI-D-13-00003.1.

Wing, S. L., and D. R. Greenwood, 1993: Fossils and fossil climate: The case for equable continental interiors in the Eocene. *Philos. Trans. Roy. Soc. B*, **341**, 243–252, https://doi.org/10.1098/rstb.1993.0109.

Zhang, L., W. W. Hay, C. Wang, and X. Gu, 2019: The evolution of latitudinal temperature gradients from the latest Cretaceous through the Present. *Earth-Sci. Rev.*, **189**, 147–158, https://doi.org/10.1016/j.earscirev.2019.01.025.

Zhu, J., C. J. Poulsen, and J. E. Tierney, 2019: Simulation of Eocene extreme warmth and high climate sensitivity through cloud feedbacks. *Sci. Adv.*, **5**, eaax1874, https://doi.org/10.1126/sciadv.aax1874.